Publisher version: 10.1021/acsanm.0c02475

Degradation Mechanism and Stability Improvement of Dopant-Free ZnO/LiF_x/Al Electron Nanocontacts in Silicon Heterojunction Solar Cells

Wenjie Lin[†‡], *Mathieu Boccard*[‡], *Sihua Zhong*[§], *Vincent Paratte*[‡], *Quentin Jeangros*[‡], *Luca Antognini*[‡], *Julie Dréon*[‡], *Jean Cattin*[‡], *Jonathan Thomet*[‡], *Zongtao Liu*[†], *Zhiming Chen*[†], *Zongcun Liang*[†//], *Pingqi Gao*[&], *Hui Shen*[*†//⊥], *and Christophe Ballif*[‡]

[†] Institute for Solar Energy Systems, Guangdong Provincial Key Laboratory of Photovoltaic Technology, School of Physics and State Key Laboratory of Optoelectronic Materials and Technologies, Sun Yat-Sen University, Guangzhou 510006, China

[‡] Photovoltaics and Thin-Film Electronics Laboratory (PV-lab), Institute of Microengineering (IMT), Ecole Polytechnique Federale de Lausanne (EPFL), Rue de la Maladière 71b, CH-2002 Neuchâtel, Switzerland

[§] School of Science, Jiangsu Ocean University, Lianyungang, Jiangsu Province 222005, China

[//] Shunde-SYSU Institute for Solar Energy, Beijiao, Shunde 528300, China

[&] School of Materials, Sun Yat-sen University, Guangzhou 510275, China

[⊥] Jiangsu Collaborative Innovation Center of Photovoltaic Science and Engineering, Changzhou University, Changzhou 213164, Jiangsu Province, China

KEYWORDS

Silicon solar cells, heterojunction, dopant free, carrier selective nanocontact, degradation mechanism, improved stability

ABSTRCT

Dopant-free passivating contacts for photovoltaics have the potential to be deposited at low costs, while providing excellent surface passivation and low contact resistance. However, one pressing issue of dopant-free carrier selective contacts is their lower environmental stability compared to conventional silicon-based contacts. In this contribution, we study the degradation in ZnO/LiF_x/Al electron selective nanocontact with experiments and simulations, and suggest design modifications for higher performance and stability. Using a thicker metallization and optimal ZnO deposition temperature (130 °C), we improved open-circuit voltage and fill-factor, together with improved stability with a retention of over 93% and 88% of the initial open-circuit voltage and fill-factor after storage in air for 380 h. The champion device has reached the efficiency of 21.3% with V_{OC} of 727 mV, J_{SC} of 37.6 mA/cm^2, and *FF* of 78.0%. Furthermore, the enhanced stability in vacuum, STEM images, and the current-exchange simulation suggests that the degradation of the a-Si: H(i)/ZnO/LiF_x/Al contact is caused by a drop of the LiF_x/Al work function, due to interaction with air. This work has ~~first~~ developed a deep understanding of degradation mechanism and the methodology of stability analysis for dopant-free silicon solar cells.

Introduction

Extensive attention has been paid to carrier selective contacts in the fields of photovoltaics, thin-film transistors and light-emitting diodes. These contacts enable asymmetric conductivity of photogenerated holes and electrons towards the opposite metallic terminals.[1] Typically, conventional heavily doped carrier selective contacts in industrial silicon solar cells are limited by Auger recombination, free-carrier absorption losses and/or high-temperature doping process (> 800 °C).[2, 3] An alternative strategy for fulfilling excellent surface passivation and a low-resistance contact simultaneously is the application of passivating contacts.[4] Remarkably, the incorporation of doped and intrinsic hydrogenated amorphous silicon (a-Si: H) stacks or polycrystalline silicon (poly-Si) combined with interfacial SiO_2 layer at the metal/silicon interface demonstrated high open-circuit voltage (V_{OC}) over 726 mV and certificated efficiency over 26%.[5, 6] However, these high efficiencies were obtained with all-back-contacted devices, due to inherent trade-offs in terms of optical and electrical performances for such contacts. Furthermore, the higher production cost of such technologies compared to traditional ones precludes so far the widespread commercialization of these technologies.[7, 8]

Dopant-free passivating contacts, composed of nanoscale non-silicon materials with a wide bandgap and a high or low work function, ~~usually~~ combined to a-Si: H(i), SiO_x or organic materials passivation layers, have been proposed as a potentially cheaper and more efficient strategy, allowing low temperature and simpler deposition methods.[9-11] Numerous high-work-function-materials have been developed to form hole selective contacts on p-Si or n-Si wafers, including transition-metal oxides (e.g., MoO_3,[10, 12] V_2O_5,[11, 13] WO_3,[14] CrO_3,[15] NiO,[16] CuO[17]), metal iodide (e.g., CuI)[18] and poly(3,4-ethylenedioxythiophene):polystyrenesulfonate (PEDOT:PSS)[19, 20].

Recently, a remarkable efficiency of 23.5% was reached for silicon heterojunction solar cells using hole-collecting and transparent MoOx (4 nm) to replace a-Si: H(p).[21] Additionally, wide variety of electron selective contact materials, such as metals (e.g., Ca,[22] Mg, Sc,[23] Yb[24]), metal oxides (e.g., MgO,[25] TiO_2,[26] ZnO,[12] Ta_2O_x,[27] BaO_x,[28] and Nb_2O_5[29]), metal nitrides (e.g., TaN_x,[30] TiN_x[31]), fluoride salts (e.g., LiF_x,[12, 26] and MgF_2[32]), carbonates (e.g., $CsCO_3$, $K_2C_xO_y$, $Rb_2C_xO_y$, CaC_xO_y, SrC_xO_y, and BaC_xO_y),[33,34] and their stack combination,[26, 35] have been successfully inserted between metal and n-Si, to reduce Schottky barrier and eliminate Fermi level pinning effect at Al/n-Si interface. Moreover, full dopant-free silicon solar cell technologies utilizing dopant-free hole and electron transport layers simultaneously, have the potential to be high-efficiency and low-cost technique in the field of industrial silicon solar cells. [12, 32]

The 19.4%-efficient dopant-free asymmetric heterocontact (DASH) silicon solar cells, applying MoO_x and LiF_x based nanocontacts with a-Si: H(i) passivation layers, was the first relevant-efficiency device produced.[36] Subsequently, the incorporation of a protective TiO_2 (1.5 nm) film between the a-Si: H passivation layer and the low work function LiF_x/Al electrode improved the efficiency (20.7%), thermal and ambient stability.[26] In another approach, by introducing the ZnO (75 nm) interlayer between a-Si: H(i) and LiF_x, the full dopant-free silicon solar cells have demonstrated a higher short circuit current (J_{SC}) and an impressive efficiency of 21.4%, attributed to the mitigated plasmonic absorption of the rather thick ZnO films.[12] Nevertheless, the ZnO/LiF_x/Al electron selective contacts exhibit severe degradation, which was also observed in ZnO-based perovskite solar cells and dye-sensitized solar cells,[37-39] limiting the deployment of dopant-free carrier selective contact technology. Besides, publications of dopant-free carrier selective contacts for silicon solar cells, lack detailed stability study and deep mechanism understanding of device degradation.

In this contribution, detailed experimental research of degradation in the ZnO/LiF_x/Al electron selective nanocontacts was conducted. We have evidenced the importance of the metallization and deposition temperature during ZnO growth, to enhance environmental stability in air. The implied-V_{OC} (iV_{OC}), contact resistance (ρ_c), and current-voltage (*J*-*V*) measurements of the ZnO/LiF_x/Al electron contacts were investigated with ageing time and in different environments. AFORS-HET simulation, scanning transmission electron microscopy (STEM), *J*-*V* measurements in the range of -2–2 V, and their analysis with an exchange current density model allowed a deep understanding of degradation mechanism and the methodology development of stability analysis.[40]

Results and Discussion

Implied V_{OC} and Contact resistance

To evaluate the passivation quality of the a-Si: H(i)/ZnO/LiF_x/Al nanocontacts aged in air, ZnO films with different deposition temperature were low-pressure chemical vapor deposited (LPCVD), using diethylzinc and water vapours as precursors, capped with 1.5 nm LiF_x/5 nm Al evaporated, as schematically shown in Figure 1a. The increase in ZnO deposition temperature improves the iV_{OC} and effective lifetime (τ_{eff}), as shown in Table 1. As shown in Table 2, fitting the lifetime curves with the model developed by Olibet et al.[41] indicates that the enhancement of iV_{OC}, attributed to a reduction of the effective surface recombination velocity (S_{eff}), is due to an increase in the fixed positive charge density (Q_f) and a decrease in the defect density (D_t) of the interface between n-Si and a-Si: H(i)/ZnO/LiF_x/Al contact. The drop of D_t could be linked to the slight decrease of Urbach energy, as shown in the photothermal deflection spectra of ZnO/a-Si: H(i) on glass (Figure S1). When ZnO deposition temperature increases further than 130 °C, the τ_{eff}, iV_{OC}, S_{eff}, Q_f and D_t remain constant. The variations of Q_f and D_t with temperature correlate

with the crystallite-size increase and the resistivity decrease of LPCVD ZnO.[42] Finally, Figure 1b shows that the iV_{OC} of a-Si: H(i)/ZnO/LiF_x/Al-nanocontacted devices is stable for up to 400 h for all ZnO deposition temperatures investigated here.

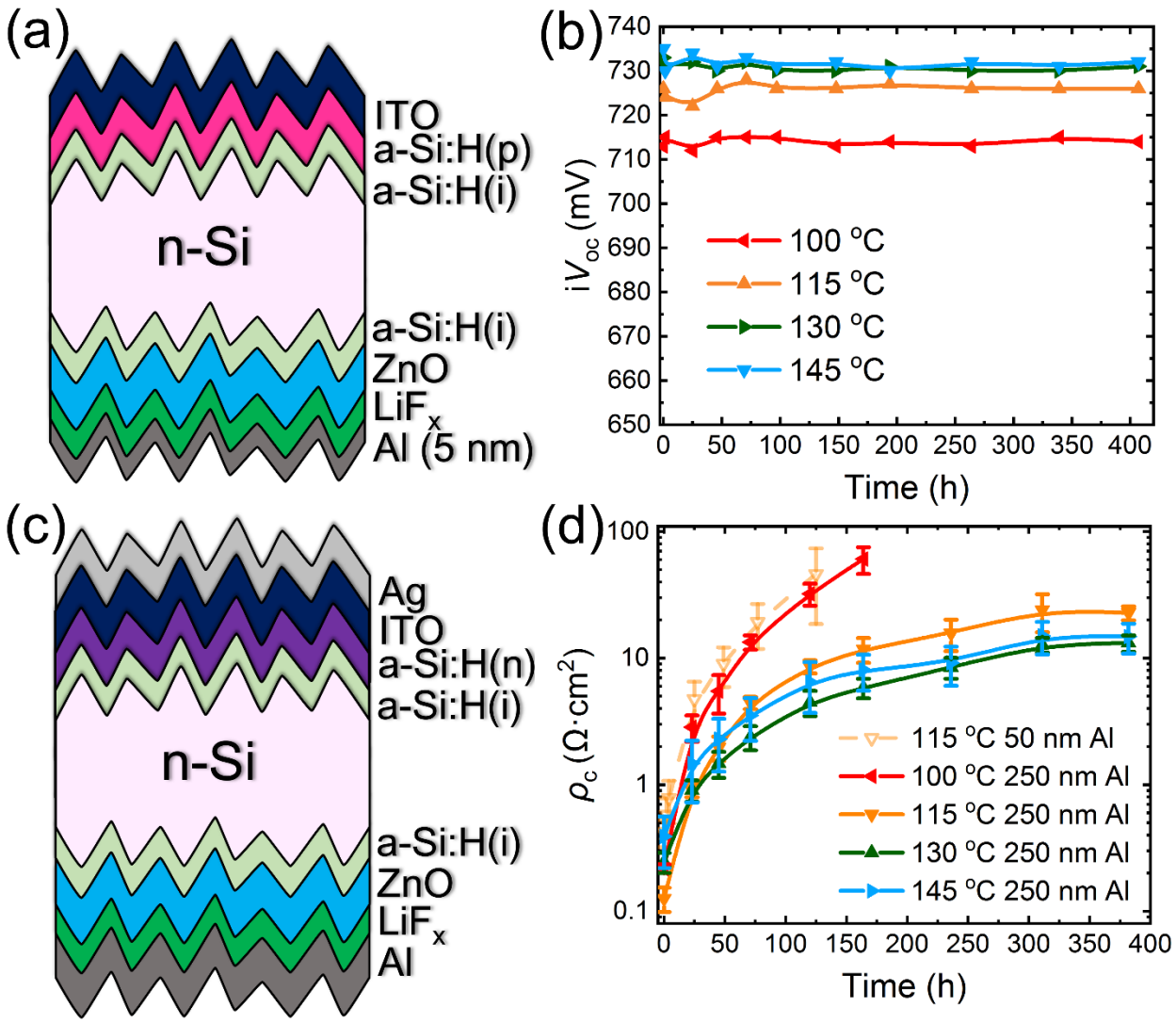

Figure 1. Implied V_{OC} characterizations and contact resistance measurements as a function of ageing time. (a) Schematic of iV_{OC} test structures with indium tin oxide (ITO)/a-Si: H(p)/a-Si: H(i)/n-Si/a-Si: H(i)/ZnO/LiF_x/Al (5 nm). (b) iV_{OC} of the samples with a series of ZnO deposition temperature. (c) Schematic view of contact resistance test structures. (d) ρ_c between n-Si and a-Si:

H(i)/ZnO/LiF_x/Al, featuring different thickness of Al (0 and 200 nm) and various ZnO deposition temperature.

Table 1. The initial iV_{OC}, ρ_c and device parameters of the samples featuring different ZnO deposition temperature.

Deposition temperature/°C	**iV_{OC}/mV**	**ρ_c/Ω·cm^2**	**V_{OC}/mV**	***FF*/%**
100	713	0.22	711.9	72.0
115	726	0.13	711.8	74.4
130	733	0.24	716.8	74.7
145	735	0.39	714.8	70.9

Table 2. The initial recombination parameters and interface electronic properties of the samples with different ZnO deposition temperature.

Deposition temperature/°C	**S_{eff}/cm·s^{-1}**	**τ_{eff}/s**	**Q_f/cm^{-2}**	**D_t/cm^{-3}**
100	26	7.0×10^{-4}	1.0×10^{9}	1.1×10^{10}
115	16	1.1×10^{-3}	9.8×10^{9}	7.9×10^{9}
130	6.5	2.2×10^{-3}	1.8×10^{10}	3.6×10^{9}
145	6.5	2.2×10^{-3}	1.8×10^{10}	3.6×10^{9}

The contact resistance was determined from the test structure, covered with nanoscale a-Si: H(i)/a-Si: H(n)/ITO/Ag and a-Si: H(i)/ZnO/LiF_x/Al at the front and rear side, respectively, depicted in the Figure 1c.[12] Table 1 shows that when the deposition temperature increases from 100 to 115 °C, ρ_c first decreases and then increases as the temperature exceeds 115 °C. It again

correlates with the larger crystal grains and decreased resistivity of ZnO layers deposited at such temperatures, and the transition of morphological surface and grain orientation in this 115–145 °C temperature range.[42] The original ρ_c with various ZnO deposition temperature are extracted to be 0.13–0.39 Ω·cm^2, which are sufficiently low to form a high-efficiency n-Si solar cell with full area heterocontact. [27 27 27 27 27 27 27, 40] As can be seen in Figure 1d, the samples with a deposition temperature of 115 °C and 50 nm thermally evaporated Al, exhibit the fastest deteriorating contact resistance by over two orders of magnitude within 130 h. By contrast, the further application of 200 nm electron beam deposited (EBD) Al in a-Si: H(i)/ZnO/LiF_x/Al contact significantly mitigated the degradation, which may be due to the further protection against air exposure. Interestingly, As the ZnO deposition temperature increases from 100 to 130 °C, the degradation rate of ρ_c decreases. The best samples with a ZnO deposition temperature of 130 °C and thicker metallization display the nearly constant ρ_c below 14 Ω·cm^2 after ageing in air for 380 h.

Device performance

Silicon heterojunction solar cells using a-Si: H(i)/ZnO/LiF_x/Al electron nanocontacts as full-area rear contacts were fabricated, as sketched in Figure 2a. Note that the same thickness of ZnO films was applied in the fabrication of all the samples. The J_{SC} was therefore similar, and since it was also in time, we focus in the following on the V_{OC} and fill factor (*FF*) of the devices with different ZnO deposition temperatures. Looking first at initial results, Table 1 shows that increasing the deposition temperature from 100 °C to 130 °C improves the V_{OC} and *FF*. Further temperature increase reduces the V_{OC} and *FF*. Moreover, the champion cells using a-Si:H(i)/ZnO (130 °C)/LiF_x/Al (250 nm) electron contacts achieved the efficiency of 21.3%, accompany with V_{OC} of 727 mV, J_{SC} of 37.6 mA/cm^2 and *FF* of 78.0%, as shown in Figure 2b. Furthermore, cell

performance with different thickness of Al (0 and 200 nm) and various ZnO deposition temperature as ageing time, are shown in Figure 2c,d. Compared with the cells with 50 nm Al whose V_{OC} and *FF* degraded drastically to 428 mV and 46.5 % within 75h, the great improvement of the device stability was found by introducing thicker metallization. Additionally, the device stability was improved as the ZnO deposition temperature increases from 100 °C to 130 °C and then was deteriorated when the temperature increases further. The trends of V_{OC} and *FF* are essentially consistent with the change of the relative contact resistance. The most stable cells (130 °C) with 250 nm Al remained above 93% of the starting V_{OC} and above 88% of the starting *FF* after aged for 380 h.

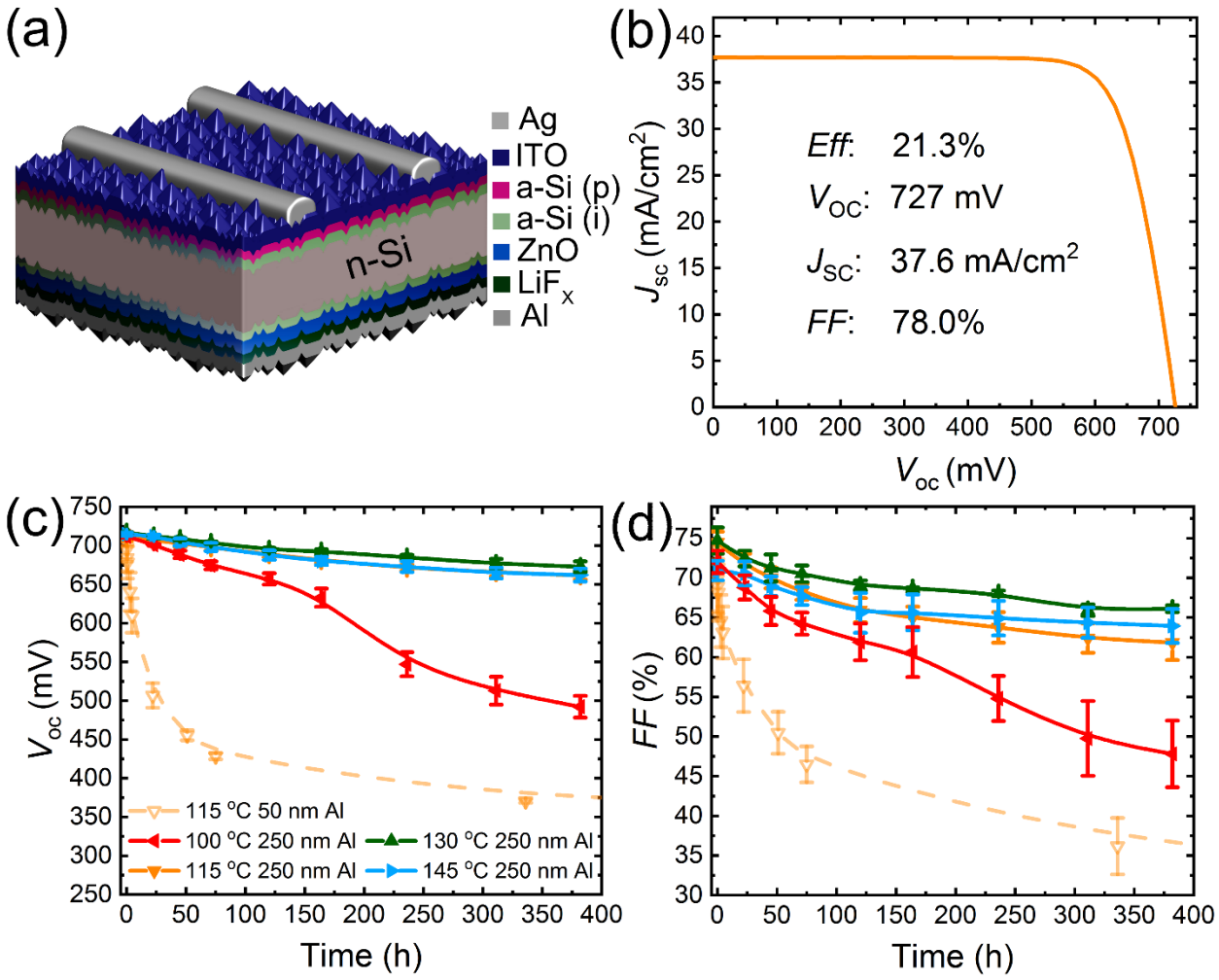

Figure 2. Device results of Silicon heterojunction solar cells featuring a-Si: H(i)/ZnO/LiF_x/Al contact. (a) Sketches of the Silicon heterojunction solar cells. (b) *J-V* curve of the champion cells using a-Si:H(i)/ZnO (130 °C)/LiF_x/Al (250 nm) electron contact. The device parameters are included in inset. (c) V_{OC} and (d) *FF* of the devices with Al thickness (0 and 200 nm) and different ZnO deposition temperature, as a function of ageing time.

Degradation mechanism

In order to understand the degradation mechanism of the a-Si: H(i)/ZnO/LiF_x/Al nanocontacts, cells with 250 nm Al were stored in both vacuum and air, then measured with ageing time,

described in the Figure 3a,b. Compared with the samples in air, the cells stored in vacuum showed an enhanced stability and retained 97% and 93% of the initial V_{OC} and *FF*, respectively, after 400 h ageing. This remaining slight degradation could be ascribed to the time spent out of vacuum for various measurements. The improved stability of the sample held in vacuum suggests that the interaction of the ZnO/LiF_x/Al nanostack with air is responsible for this degradation, which is consistent with the fact mentioned above that the use of thicker metal protection mitigated the degradation. Thus, an encapsulated module with a-Si: H(i)/ZnO/LiF_x/Al electron selective contacts has the potential to demonstrate sufficient stability in air. STEM bright-field (BF), high-angle annular dark-field (HAADF) images and corresponding energy-dispersive X ray spectra (EDX) data of the a-Si: H(i)/ZnO/LiF_x/Al (~ 100 nm) nanocontact after the exposure of 432 h in air (thus after strong degradation) are shown in Figure 3c-f. The EDX signal of the F K edge highlights the presence of the LiF_x interlayer separating the ZnO from Al. The existence of O in the LiF_x/Al layer might be attributed to air ingress. The presence of O is also likely to result from the oxidation of the surfaces of the thin TEM lamella in-between or during process steps. In addition, as referred in Table S1, the reaction calculator also suggests that Al can reacts with air in a-Si: H(i)/ZnO/LiF_x/Al contacts,[43] leading to the work function increase of LiF_x/Al, which is consistent with the AFORS-HET simulation (Figure S2).[44] The capping-layer work function was shown critical to the performance of ZnO-based nanocontacts, thus such an increase is likely to be the origin of the degradation of ρ_c, V_{OC} and *FF*. Although Al is known to form a self-limiting very thin oxide layer preventing diffusion of oxygen, permeation or percolation of oxygen-containing molecules through the Al film is a possible mechanism.

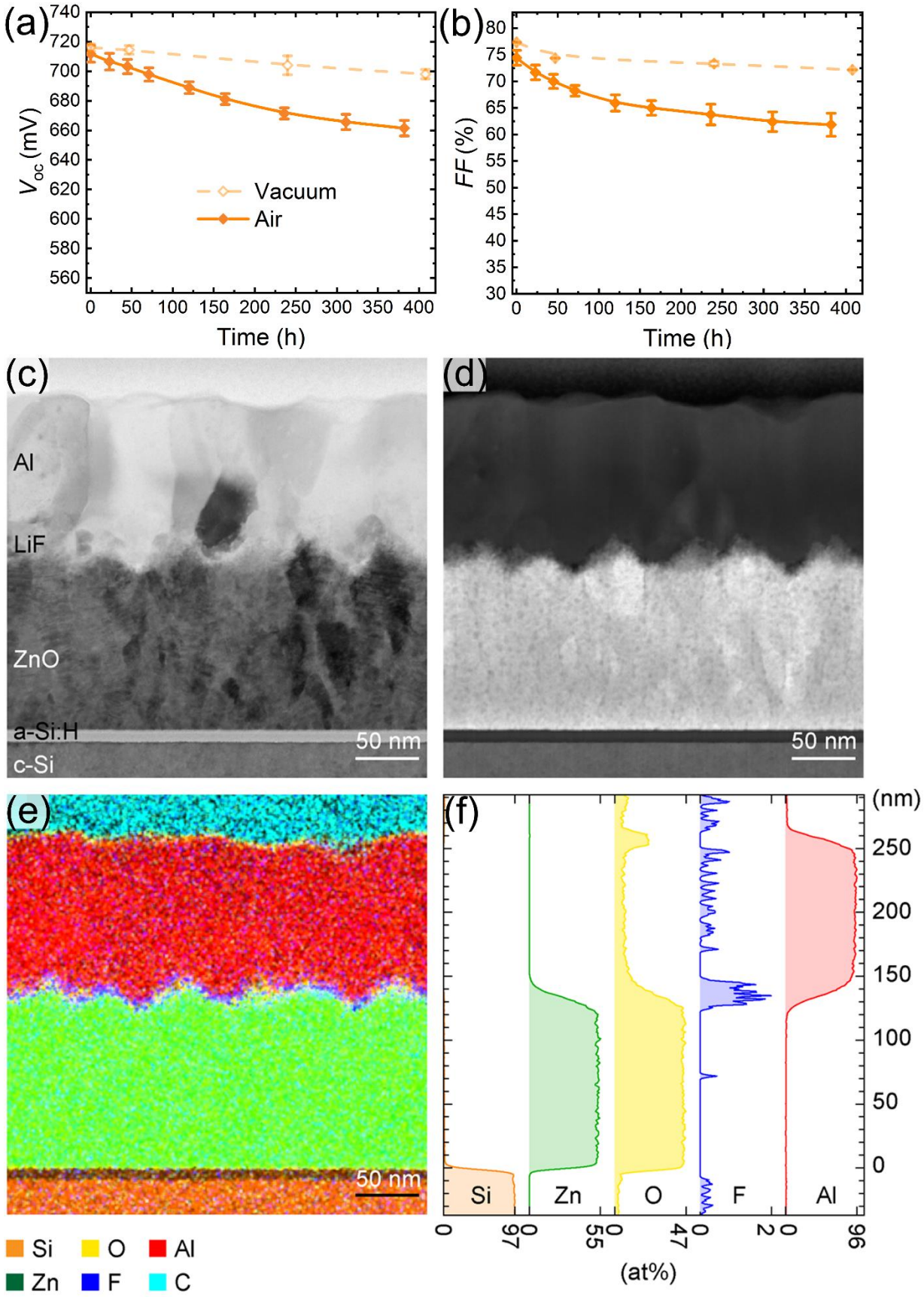
(a)
740
720
700
680
660
640
620
600
580
560
V_{oc} (mV)
Vacuum
Air
0 50 100 150 200 250 300 350 400
Time (h)
(b)
80
75
70
65
60
55
50
45
40
35
30
FF (%)
0 50 100 150 200 250 300 350 400
Time (h)
(c)
Al
LiF
ZnO
a-Si:H
c-Si
50 nm
(d)
50 nm
(e)
50 nm
Si
O
Al
Zn
F
C
(f)
(nm)
250
200
150
100
50
0
Si
Zn
O
F
Al
0 97
0 55
0 47
0 2
0 96
(at%)

Figure 3. The degradation mechanism analysis of a-Si: H(i)/ZnO/LiF_x/Al electron contacts. (a) V_{OC} and (b) *FF* of the cells in vacuum and air, as a function of ageing time. STEM microscopy images of a-Si: H(i)/ZnO/LiF_x/Al (~ 100 nm) electron contacts. (c) STEM BF, (d) HAADF images, (e) Cross-sectional STEM EDX map, and (f) corresponding of atomic concentration profile, computed from the the Si, Zn, O, F and Al K edges.

S-shaped *J-V* curve

In view of the difficulty of accessing the cause of the degradation from the composition or structural analysis, we performed a more detailed analysis of the *J-V* curve at various stages of degradation. The *J-V* curves of the devices with a-Si: H(i)/ZnO (115 °C)/LiF_x/Al (250 nm) electron nanocontacts exhibit standard diode characteristics shape, with decline of V_{OC} and FF as ageing time, illustrated in Figure 4a. Interestingly, the *J-V* curves measured in the test range of 1–2 V were found to turn to S shape with ageing time, as shown in Figure 4b. The transition of the tested *J-V* curves as ageing time increase is basically consistent with the change of the simulated *J-V* curves with the increasing work function of LiF_x/Al by AFORS HET, as shown in Figure S3. Then, the devices after the 2088 h storage were measured at various illuminations and temperatures, as shown in Figure 4c and 4d, respectively. As the illumination decreases, the S-shaped *J-V* curves get more pronounced. However, the S-shaped *J-V* curves vanish with the temperature increasing.

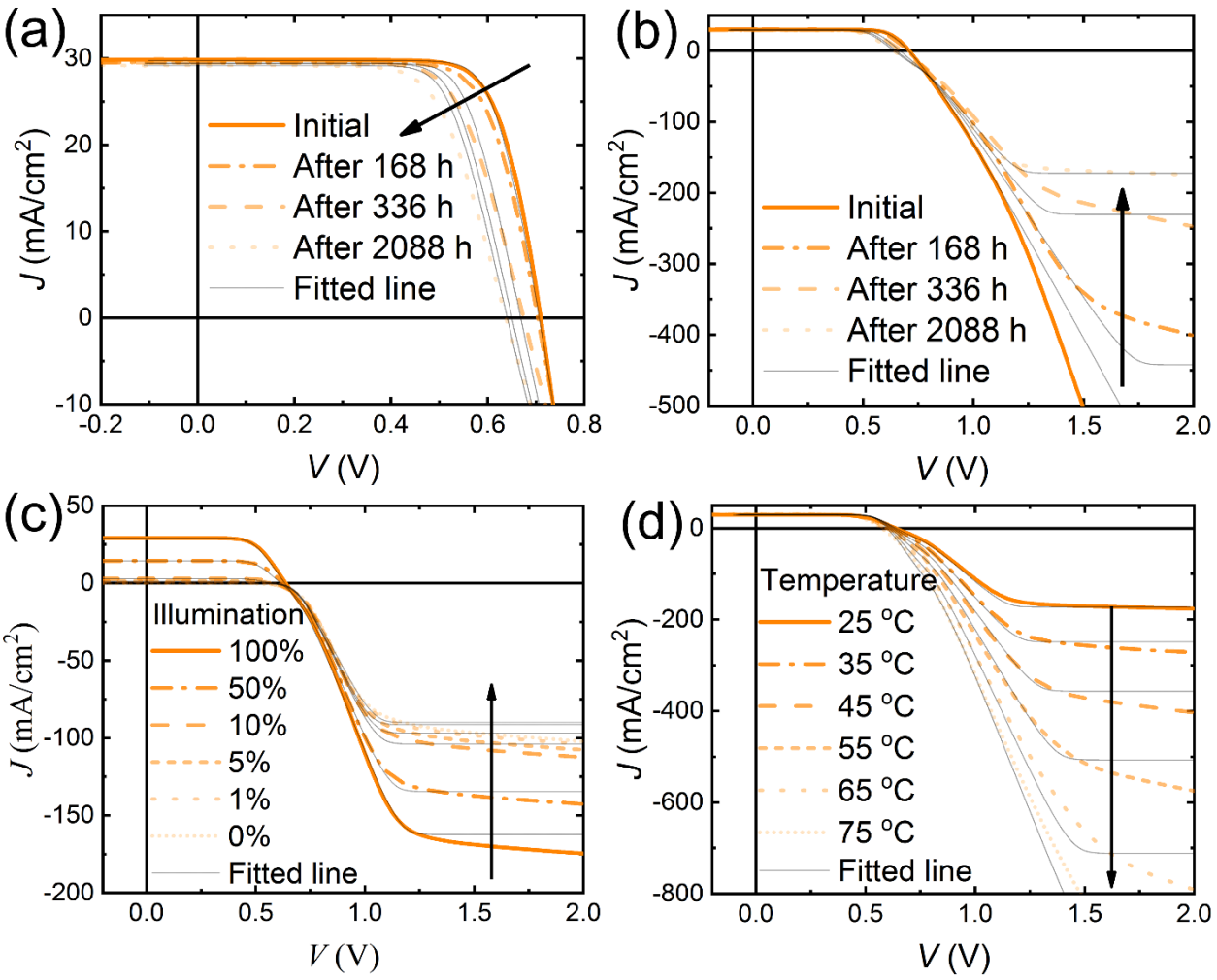

Figure 4. S-shaped *J-V* curves of the devices with a-Si: H(i)/ZnO/LiF_x/Al electron selective contacts using deposition temperature of 115 °C and 250 nm Al. The *J-V* curves as a function of ageing time, in the range of (a) -0.2–0.8 V and (b) -0.2–2 V. The S-shaped *J-V* curves of the samples after 2088h, varying (c) illumination ratio of 100 mW/cm^2 with fixed temperature of 25 °C and (d) temperatures with fixed illumination of 100 mW/cm^2. The fitted lines were reproduced using exchange current density model.

For further understanding of the S-shaped *J-V* curves, an exchange current density model,[40] was utilized to reproduce our current-voltage trends. This model, sketched in Figure 5a, describes the

characteristics of contact-limited solar cells with the flows of both electrons and holes through each of their contacts. There are therefore four saturation current densities (two per contacts) representing the Ag/ITO/a-Si: H(p)/a-Si: H(i) hole contact on the one hand ($\boldsymbol{J_{0h}^{p}}$ and J_{0e}^{p}), and a-Si: H(i)/ZnO/LiF_x/Al electron contact on the other hand (J_{0h}^{ZnO} and $\boldsymbol{J_{0e}^{ZnO}}$). The *J-V* characteristics of the cell under the assumptions are

$$J(V) = -\left(J_L + J_{0e}^{p} + J_{0h}^{ZnO}\right) + \frac{J_L + J_{0e}^{p} + \boldsymbol{J_{0e}^{ZnO}}}{1 + \frac{\boldsymbol{J_{0e}^{ZnO}}}{J_{0e}^{p}} e^{-V/V_T}} + \frac{J_L + J_{0h}^{ZnO} + \boldsymbol{J_{0h}^{p}}}{1 + \frac{\boldsymbol{J_{0h}^{p}}}{J_{0h}^{ZnO}} e^{-V/V_T}} \ , \tag{1}$$

Here, $V_T = k_B T/q$, is the thermal voltage, where k_B is the Boltzmann constant, T is the temperature, q is the electron charge. The corresponding J_0's are

$$\boldsymbol{J_{0h}^{p}} = A_h^* T^2 e^{-(E_V - \varphi^p)/k_B T} \ , \tag{2}$$

$$J_{0e}^{p} = A_e^* T^2 e^{E_C - \varphi^p/k_B T} \ , \tag{3}$$

$$J_{0h}^{ZnO} = A_h^* T^2 e^{-(E_V - \varphi^{ZnO})/k_B T} \ , \tag{4}$$

$$\boldsymbol{J_{0e}^{ZnO}} = A_e^* T^2 e^{E_C - \varphi^{ZnO}/k_B T} \ , \tag{5}$$

Where, A^* is the Richardson constant, A_e^* and A_p^* can be different, E_C and E_V are the conduction- and valence-band energies of silicon, and φ^p and φ^{ZnO} are work-function energies of Ag/ITO/a-Si: H(i)/a-Si: H(p) contact and a-Si: H(i)/ZnO/LiF_x/Al contact, respectively. The effective A^* can be calculated for metal Schottky contacts according to:

$$A_h^* = \frac{4\pi m_h^* k_B^2 q}{h^3} \ , \tag{6}$$

$$A_e^* = \frac{4\pi m_e^* k_B^2 q}{h^3} \ , \tag{7}$$

where h is Planck's constant, and m^* is the carrier effective mass, given by

$$m_h^* = \frac{h^2}{2\pi k_B T}\left(\frac{N_v}{2}\right)^{2/3}, \quad (8)$$

$$m_e^* = \frac{h^2}{2\pi k_B T}\left(\frac{N_c}{2}\right)^{2/3}. \quad (9)$$

An Ohmic series resistance was added to the model, which was slightly adjusted to reproduce the slope at high-forward bias between 0.7 and 2.4 Ω cm^2 as shown in Figure 5b-d. Also, since the contacts used here rely on heterostructures and are by far not ideal Schottky contacts, equations (6) and (7) are not expected to be applicable, although the general formalism is applicable.[40] Thus, the dependency of A^* with $1/T$ was maintained, and equations (2) to (5) can be rewritten as:

$$\boldsymbol{J_{0h}^p = a_{0h}^p T e^{-(E_V-\varphi^p)/k_B T}}, \quad (10)$$

$$J_{0e}^p = a_{0e}^p T e^{E_C-\varphi^p/k_B T}, \quad (11)$$

$$J_{0h}^{ZnO} = a_{0h}^{ZnO} T e^{-(E_V-\varphi^{ZnO})/k_B T}, \quad (12)$$

$$\boldsymbol{J_{0e}^{ZnO} = a_{0e}^{ZnO} T e^{E_C-\varphi^{ZnO}/k_B T}}. \quad (13)$$

Table S2 shows the values chosen for the a_0 parameters to fit all curves. These enabled a good fit of the data while appearing physically realistic. Then, most of the parameters were kept constant for all *J-V* curves exhibited in Figure 4: Only the work-function of the a-Si: H(i)/ZnO/LiF$_x$/Al contact (φ^{ZnO} increases from 4.22 eV to 4.3 eV as ageing time) was varied to reproduce the effect of degradation in Figure 4a,b, whereas only T was changed to reproduce the effect of changing the temperature for curves shown in Figure 4d (as well as E_C to reproduce the temperature dependency of the Si bandgap[45]). Finally, when changing illumination, J_L and J_{0h}^p were varied proportionally to the illumination, the latter accounting for the large change in hole density in the absorber. Conversely, $\boldsymbol{J_{0e}^{ZnO}}$ was only slightly reduced by 20% with illumination since the electron

density changes much less in the n-type wafer used here. Resulting values for J_0's are shown in Figure 5b-d, with the varying parameters indicated in the graph. As can be seen in Figure 4, the agreement with the experiment is excellent in all cases besides a few parameters (J_L, T and φ_0^{ZnO}) variations. Notably, this model enables reproducing the current saturation in forward bias conditions, which can not be fitted with a typical diode model, making it valuable for S-shaped *J-V* curve analysis. This model is therefore consistent with our interpretation that an increase of the work function of the contact is causing the observed degradation.

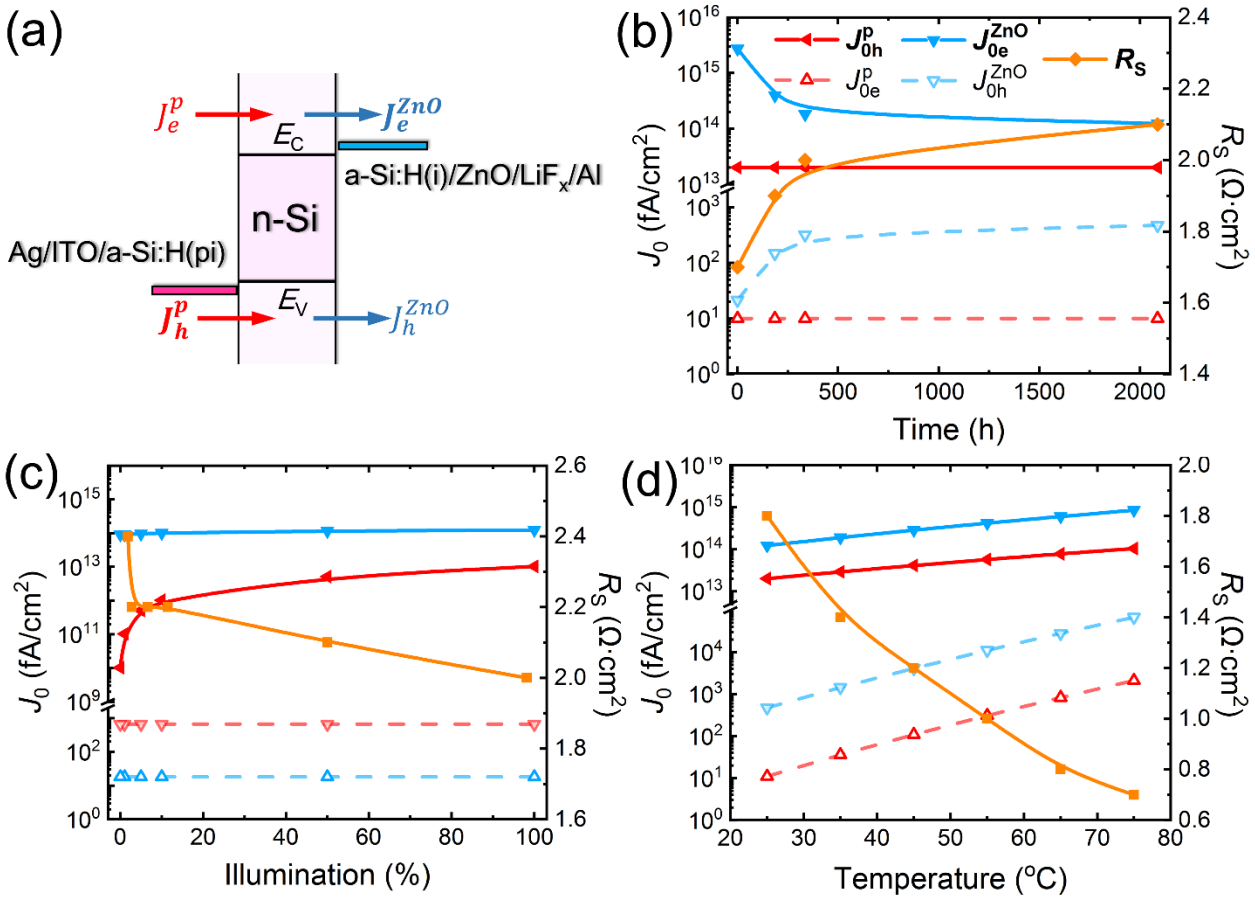

Figure 5. Exchange current density model analysis of the device with Ag/ITO/a-Si: H(p)/a-Si: H(i) hole contact and a-Si: H(i)/ZnO/LiF$_x$/Al electron contact. (a) Schematic description, which consists of four electron and hole equilibrium exchange current densities. The $\boldsymbol{J_{0h}^p}, J_{0e}^p, J_{0h}^{ZnO}, \boldsymbol{J_{0e}^{ZnO}}$

and R_S fitted from *J-V* curves shown in Figure 4, as a function of (b) ageing time, (c) illumination and (d) temperature.

4. Conclusion

In this work, we investigated the ambient stability of the a-Si: H(i)/ZnO/LiF_x/Al passivating electron nanocontact in terms of passivation, contact resistivity and cell performance. The iV_{OC} remained stable, but the V_{OC} and *FF* degraded with ageing time, matching well to the trend of the ρ_c. The employment of thicker Al and optimized ZnO deposition (130 °C) improved the iV_{OC}, ρ_c, V_{OC}, *FF* and stability, which maintained above 93% of their initial V_{OC} and above 88% of the initial *FF* after ageing for 380 h. Moreover, the champion cells with the efficiency of 21.3%, V_{OC} of 727 mV, J_{SC} of 37.6 mA/cm2, and *FF* of 78.0% was demonstrated. Furthermore, the enhanced stability in vacuum and STEM images revealed that the degradation of the a-Si: H(i)/ZnO/LiF_x/Al contact is caused by the air ingress in LiF_x/Al interface, indicating potentially excellent stability for the encapsulated module with a-Si: H(i)/ZnO/LiF_x/Al nanocontacts. Finally, AFORS-HET simulation, current-exchange modeling and S-shaped *J-V* characteristics in the range of 1–2 V disclosed that the deteriorated work function of LiF_x/Al is responsible for the degradation.

Experimental Section

For the iV_{OC} characterization, the samples were fabricated on n-type float zone (FZ) c-Si substrates with a thickness of ~ 195 μm and resistivity of ~ 2.1 Ω cm. Both sides of the textured and cleaned wafers were covered with a plasma-enhanced chemical vapor deposited (PECVD) a-Si: H(i) layer (~ 9 nm on the flat reference glass). Then, on the front side, a-Si: H(p) (~ 10 nm) and ITO (~ 75 nm) were grown by PECVD and magnetron sputtering, respectively, followed by

annealing at 210 °C. Subsequently, ZnO films were deposited at the rear side via LPCVD at variable deposition temperature (100–145 °C). Note that the thickness of all the ZnO layers was set to ~ 140 nm, requiring to adjust the deposition time, due to more thermal energy at higher temperatures, resulting in accelerated ZnO growth.[42] The samples were annealed at 150 °C for 30 min, followed by thermal evaporation of LiF_x (~ 1.5 nm)/Al (~ 5 nm). Finally, iV_{OC} measurements were taken using Sinton Instruments WCT120.

The contact resistance measurements were conducted using textured FZ n-Si wafers, covered with PECVD a-Si: H(i)/a-Si: H(n) (~ 10 nm) and a-Si: H(i) on the front and back sides, respectively. The ITO/Ag stacks were sputtered on the front side, before annealing at 210 °C. Here, the contact between Ag/ITO/a-Si: H(n)/a-Si: H(i) and n-Si was shown to be Ohmic contact with a contact resistance of 0.02 Ω cm^2 in our previous work.[12] In the following, annealing at 150 °C was implemented after the deposition of LPCVD ZnO at the rear surface. LiF_x/Al (~ 50 nm) was evaporated on the rear side through a mask of 0.75 × 0.75 cm^2, subsequently capped by EBD Al (0 or 200 nm) without breaking the vacuum. The dark *J-V* curves were acquired by a Keithley 2601A source meter.

Silicon heterojunction solar cells with a-Si: H(i)/ZnO/LiF_x/Al were processed, employing samples covered with a-Si: H(i)/a-Si: H(p) and a-Si: H(i) on the front and back surfaces, respectively similar to the lifetime samples. The sputtering of ITO was carried out through a mask to define 2 × 2 cm^2 area, followed by screen printing of Ag grid and curing at 210 °C. LPCVD ZnO was deposited on the rear side, followed by an annealing at 150 °C. Finally, the thermal evaporation of LiF_x/Al and electron beam deposition of Al were performed, similar to the contact resistance structures. The light *J-V* behaviors were obtained under standard test condition (100 mW/cm^2, AM 1.5 spectrum, and 25 °C), by the utilization of a Wacom WXS-90S-L2 solar

simulator. Additional light *J-V* curves in the range of -2–2 V were measured under an illumination of 100 mW/cm^2 at variable temperature (25–75 °C) and under variable illumination intensity (0–100 mW/cm^2) at 25 °C.

The microstructure of the a-Si: H(i)/ZnO/LiF_x/Al (~ 100 nm) nanocontact stack, here deposited on a polished <100> n-Si wafer and stored in air for 18 days, was assessed in cross-section by STEM. A thin lamella was prepared using the conventional focused ion beam lift-out method in a Zeiss NVision 40 using a final gallium beam milling voltage of 5 kV. STEM BF, HAADF images and EDX were obtained using a Fisher Scientific Osiris microscope operated at 200 kV with a beam current of 250 pA and equipped with four silicon drift detectors for fast EDX mapping. EDX data was quantified using the Cliff-Lorimer method.[46]

ASSOCIATED CONTENT

Supporting Information

The feasibility of the reactions between the materials in the a-Si: H(i)/ZnO/LiF_x/Al nanocontact and air. The AFORS-HET simulation of the Silicon heterojunction solar cells using a-Si: H(i)/ZnO/LiF_x/Al contact, as function of the work function of LiF_x/Al. The value of a_0's parameter for the exchange current density model.

AUTHOR INFORMATION

Corresponding Author

*Email: shenhui1956@163.com

Notes

The authors declare no competing financial interest.

ACKNOWLEDGMENTS

The authors thank all group members in PV-lab, EPFL, and funding from Swiss national science foundation under Ambizione Energy grant ICONS (PZENP2_173627). This work was partly supported by the National Natural Science Foundation of China (Grant Nos. 61774173, 61974169, 62034009 and 61774171), the Guangzhou Collaborative Innovation Major Project of producing, teaching and researching (Grant No. 201508010011), the Jiangsu Collaborative Innovation Center of Photovoltaic Science and Engineering (Grant No. SCZ1405500002), the Natural Science Foundation for Distinguished Young Scholars of Guangdong Province (Grant No. 2019B151502053)

REFERENCES

(1) Melskens, J.; van de Loo, B. W.; Macco, B.; Black, L. E.; Smit, S.; Kessels, W., Passivating contacts for crystalline silicon solar cells: From concepts and materials to prospects. *IEEE J. Photovoltaics* 2018, 8, 373-388.

(2) Baker-Finch, S. C.; McIntosh, K. R.; Yan, D.; Fong, K. C.; Kho, T. C., Near-infrared free carrier absorption in heavily doped silicon. *J. Appl. Phys.* 2014, 116, 063106.

(3) Battaglia, C.; Cuevas, A.; De Wolf, S., High-efficiency crystalline silicon solar cells: status and perspectives. *Energy Environ. Sci.* 2016, 9, 1552-1576.

(4) Allen, T. G.; Bullock, J.; Yang, X.; Javey, A.; De Wolf, S., Passivating contacts for crystalline silicon solar cells. *Nat. Energy* 2019, 1-15.

(5) Yao, Z.; Cai, L.; Meng, L.; Qiu, K.; Lin, W.; Jin, J.; Duan, W.; Ding, K.; Li, S.; Ai, B.; Liang, Z.; Shen, H., High‐Performance and Stable Dopant‐Free Silicon Solar Cells with Magnesium Acetylacetonate Electron‐Selective Contacts. *physica status solidi (RRL) – Rapid Research Letters* 2020, 14, 2000103.

(6) Chen, D.; Chen, Y.; Wang, Z.; Gong, J.; Liu, C.; Zou, Y.; He, Y.; Wang, Y.; Yuan, L.; Lin, W.; Xia, R.; Yin, L.; Zhang, X.; Xu, G.; Yang, Y.; Shen, H.; Feng, Z.; Altermatt, P. P.; Verlinden, P. J., 24.58% total area efficiency of screen-printed, large area industrial silicon solar cells with the tunnel oxide passivated contacts (i-TOPCon) design. *Sol. Energy Mater. Sol. Cells* 2020, 206, 110258.

(7) Jin, G.; Widenborg, P. I.; Campbell, P.; Varlamov, S., Lambertian matched absorption enhancement in PECVD poly‐Si thin film on aluminum induced textured glass superstrates for solar cell applications. *Prog. Photovoltaics Res. Appl.* 2010, 18, 582-589.

(8) Holman, Z. C.; Descoeudres, A.; Barraud, L.; Fernandez, F. Z.; Seif, J. P.; De Wolf, S.; Ballif, C., Current losses at the front of silicon heterojunction solar cells. *IEEE J. Photovoltaics* 2012, 2, 7-15.

(9) Qiu, K.; Xie, Q.; Qiu, D.; Cai, L.; Wu, W.; Lin, W.; Yao, Z.; Ai, B.; Liang, Z.; Shen, H., Power-loss analysis of a dopant-free ZnS/p-Si heterojunction solar cell with WO3 as hole-selective contact. *Sol. Energy* 2018, 165, 35-42.

(10) Chen, J.; Shen, Y.; Guo, J.; Chen, B.; Fan, J.; Li, F.; Liu, H.; Xu, Y.; Mai, Y., Silicon surface passivation by polystyrenesulfonate thin films. *Appl. Phys. Lett.* 2017, 110, 083904.

(11) Chen, J.; Wan, L.; Li, H.; Yan, J.; Ma, J.; Sun, B.; Li, F.; Flavel, B. S., A Polymer/Carbon‐Nanotube Ink as a Boron‐Dopant/Inorganic‐Passivation Free Carrier Selective Contact for Silicon Solar Cells with over 21% Efficiency. *Adv. Funct. Mater.* 2020, 2004476.

(12) Zhong, S.; Dreon, J.; Jeangros, Q.; Aydin, E.; De Wolf, S.; Fu, F.; Boccard, M.; Ballif, C., Mitigating Plasmonic Absorption Losses at Rear Electrodes in High‐Efficiency Silicon Solar Cells Using Dopant‐Free Contact Stacks. *Adv. Funct. Mater.* 2019, 1907840.

(13) <CNT.pdf>.

(14) Ali, H.; Koul, S.; Gregory, G.; Bullock, J.; Javey, A.; Kushima, A.; Davis, K. O., Thermal Stability of Hole-Selective Tungsten Oxide: In Situ Transmission Electron Microscopy Study. *Sci. Rep.* 2018, 8, 1-5.

(15) Lin, W.; Wu, W.; Liu, Z.; Qiu, K.; Cai, L.; Yao, Z.; Ai, B.; Liang, Z.; Shen, H., Chromium Trioxide Hole-Selective Heterocontacts for Silicon Solar Cells. *ACS Appl. Mater. Interfaces* 2018, 10, 13645-13651.

(16) Lee, Y. H.; Song, H.-e.; Kim, K.-H.; Oh, J., Investigation of surface reactions in metal oxide on Si for efficient heterojunction Si solar cells. *APL Mater.* 2019, 7, 071106.

(17) Liu, Y.; Zhu, J.; Cai, L.; Yao, Z.; Duan, C.; Zhao, Z.; Zhao, C.; Mai, W., Solution‐Processed High‐Quality Cu2O Thin Films as Hole Transport Layers for Pushing the Conversion Efficiency Limit of Cu2O/Si Heterojunction Solar Cells. *Solar RRL* 2020, 4, 1900339.

(18) Lin, W.; Wu, W.; Xie, Q.; Liu, Z.; Qiu, K.; Cai, L.; Yao, Z.; Meng, L.; Ai, B.; Liang, Z., Conductive cuprous iodide hole-selective contacts with thermal and ambient stability for silicon solar cells. *ACS Appl. Mater. Interfaces* 2018, 10, 43699-43706.

(19) Wan, L.; Zhang, C.; Ge, K.; Yang, X.; Li, F.; Yan, W.; Xu, Z.; Yang, L.; Xu, Y.; Song, D., Conductive Hole‐Selective Passivating Contacts for Crystalline Silicon Solar Cells. *Adv. Energy Mater.* 2020, 1903851.

(20) He, J.; Hossain, M. A.; Lin, H.; Wang, W.; Karuturi, S. K.; Hoex, B.; Ye, J.; Gao, P.; Bullock, J.; Wan, Y., 15% Efficiency ultrathin silicon solar cells with fluorine-doped titanium oxide and chemically tailored poly (3, 4-ethylenedioxythiophene): poly (styrenesulfonate) as asymmetric heterocontact. *ACS Nano* 2019, 13, 6356-6362.

(21) Dréon, J.; Jeangros, Q.; Cattin, J.; Haschke, J.; Antognini, L.; Ballif, C.; Boccard, M., 23.5%-efficient silicon heterojunction silicon solar cell using molybdenum oxide as hole-selective contact. *Nano Energy* 2020, 104495.

(22) Cho, J.; Melskens, J.; Debucquoy, M.; Recamán Payo, M.; Jambaldinni, S.; Bearda, T.; Gordon, I.; Szlufcik, J.; Kessels, W.; Poortmans, J., Passivating electron‐selective contacts for silicon solar cells based on an a‐Si: H/TiOx stack and a low work function metal. *Prog. Photovoltaics Res. Appl.* 2018, 26, 835-845.

(23) Quan, C.; Tong, H.; Yang, Z.; Ke, X.; Liao, M.; Gao, P.; Wang, D.; Yuan, Z.; Chen, K.; Yang, J., Electron‐Selective Scandium− Tunnel Oxide Passivated Contact for n‐Type Silicon Solar Cells. *Solar RRL* 2018, 2, 1800071.

(24) Cho, J.; Melskens, J.; Payo, M. R.; Debucquoy, M.; Radhakrishnan, H. S.; Gordon, I.; Szlufcik, J.; Kessels, W.; Poortmans, J., Performance and Thermal Stability of an a-Si: H/TiO x/Yb Stack as an Electron-Selective Contact in Silicon Heterojunction Solar Cells. *ACS Applied Energy Materials* 2019, 2, 1393-1404.

(25) Yu, J.; Liao, M.; Yan, D.; Wan, Y.; Lin, H.; Wang, Z.; Gao, P.; Zeng, Y.; Yan, B.; Ye, J., Activating and optimizing evaporation-processed magnesium oxide passivating contact for silicon solar cells. *Nano Energy* 2019, 62, 181-188.

(26) Bullock, J.; Wan, Y.; Xu, Z.; Essig, S.; Hettick, M.; Wang, H.; Ji, W.; Boccard, M.; Cuevas, A.; Ballif, C., Stable dopant-free asymmetric heterocontact silicon solar cells with efficiencies above 20%. *ACS Energy Lett.* 2018, 3, 508-513.

(27) Wan, Y.; Karuturi, S. K.; Samundsett, C.; Bullock, J.; Hettick, M.; Yan, D.; Peng, J.; Narangari, P. R.; Mokkapati, S.; Tan, H. H., Tantalum oxide electron-selective heterocontacts for silicon photovoltaics and photoelectrochemical water reduction. *ACS Energy Lett.* 2017, 3, 125-131.

(28) Kim, S.-H.; Jung, J.-Y.; Wehrspohn, R. B.; Lee, J.-H., All-Room-Temperature Processed 17.25%-Crystalline Silicon Solar Cell. *ACS Applied Energy Materials* 2020, 3, 3180-3185.

(29) Macco, B.; Black, L. E.; Melskens, J.; van de Loo, B. W.; Berghuis, W.-J. H.; Verheijen, M. A.; Kessels, W. M., Atomic-layer deposited Nb2O5 as transparent passivating electron contact for c-Si solar cells. *Sol. Energy Mater. Sol. Cells* 2018, 184, 98-104.

(30) Yang, X.; Aydin, E.; Xu, H.; Kang, J.; Hedhili, M.; Liu, W.; Wan, Y.; Peng, J.; Samundsett, C.; Cuevas, A., Tantalum Nitride Electron‐Selective Contact for Crystalline Silicon Solar Cells. *Adv. Energy Mater.* 2018, 8, 1800608.

(31) Yang, X.; Liu, W.; De Bastiani, M.; Allen, T.; Kang, J.; Xu, H.; Aydin, E.; Xu, L.; Bi, Q.; Dang, H., Dual-function electron-conductive, hole-blocking titanium nitride contacts for efficient silicon solar cells. *Joule* 2019, 3, 1314-1327.

(32) Wu, W.; Lin, W.; Zhong, S.; Paviet-Salomon, B.; Despeisse, M.; Jeangros, Q.; Liang, Z.; Boccard, M.; Shen, H.; Ballif, C., Dopant‐free back contacted silicon solar cells with an efficiency of 22.1%. *physica status solidi (RRL)‐Rapid Research Letters*.

(33) Wang, F.; Zhang, Y.; Yang, M.; Yang, L.; Sui, Y.; Yang, J.; Zhao, Y.; Zhang, X., Realization of 16.9% Efficiency on nanowires heterojunction solar cells with dopant‐free contact for bifacial polarities. *Adv. Funct. Mater.* 2018, 28, 1805001.

(34) Wan, Y.; Bullock, J.; Hettick, M.; Xu, Z.; Samundsett, C.; Yan, D.; Peng, J.; Ye, J.; Javey, A.; Cuevas, A., Temperature and Humidity Stable Alkali/Alkaline‐Earth Metal Carbonates as Electron Heterocontacts for Silicon Photovoltaics. *Adv. Energy Mater.* 2018, 8, 1800743.

(35) Masmitjà, G.; Ortega, P.; Puigdollers, J.; Gerling, L.; Martín, I.; Voz, C.; Alcubilla, R., Interdigitated back-contacted crystalline silicon solar cells with low-temperature dopant-free selective contacts. *J. Mater. Chem.* 2018, 6, 3977-3985.

(36) Bullock, J.; Hettick, M.; Geissbühler, J.; Ong, A. J.; Allen, T.; Sutter-Fella, C. M.; Chen, T.; Ota, H.; Schaler, E. W.; De Wolf, S., Efficient silicon solar cells with dopant-free asymmetric heterocontacts. *Nat. Energy* 2016, 1, 1-7.

(37) Chen, P.; Yin, X.; Que, M.; Yang, Y.; Que, W., TiO 2 passivation for improved efficiency and stability of ZnO nanorods based perovskite solar cells. *RSC Adv.* 2016, 6, 57996-58002.

(38) Cao, J.; Wu, B.; Chen, R.; Wu, Y.; Hui, Y.; Mao, B. W.; Zheng, N., Efficient, Hysteresis‐Free, and Stable Perovskite Solar Cells with ZnO as Electron‐Transport Layer: Effect of Surface Passivation. *Adv. Mater.* 2018, 30, 1705596.

(39) Ke, L.; Dolmanan, S. B.; Shen, L.; Pallathadk, P. K.; Zhang, Z.; Lai, D. M. Y.; Liu, H., Degradation mechanism of ZnO-based dye-sensitized solar cells. *Sol. Energy Mater. Sol. Cells* 2010, 94, 323-326.

(40) Roe, E. T.; Egelhofer, K. E.; Lonergan, M. C., Exchange current density model for the contact-determined current-voltage behavior of solar cells. *J. Appl. Phys.* 2019, 125, 225302.

(41) Olibet, S.; Vallat-Sauvain, E.; Ballif, C., Model for a-Si: H/c-Si interface recombination based on the amphoteric nature of silicon dangling bonds. *Physical Review B* 2007, 76, 035326.

(42) Fay, S.; Kroll, U.; Bucher, C.; Vallat-Sauvain, E.; Shah, A., Low pressure chemical vapour deposition of ZnO layers for thin-film solar cells: temperature-induced morphological changes. *Sol. Energy Mater. Sol. Cells* 2005, 86, 385-397.

(43) Material project, Reaction calculator. https://materialsproject.org/#apps/interfacereactions/, 2019 (accessed 15 November 2019).

(44) Varache, R.; Leendertz, C.; Gueunier-Farret, M.; Haschke, J.; Muñoz, D.; Korte, L., Investigation of selective junctions using a newly developed tunnel current model for solar cell applications. *Sol. Energy Mater. Sol. Cells* 2015, 141, 14-23.

(45) Mönch, W.; Enninghorst, R.; Clemens, H., An experimental study on the temperature dependence of electron affinity and ionization energy at semiconductor surfaces. *Surf. Sci. Lett.* 1981, 102, L54-L58.

(46) Cliff, G.; Lorimer, G. W., The quantitative analysis of thin specimens. *J. Microsc.* 1975, 103, 203-207.

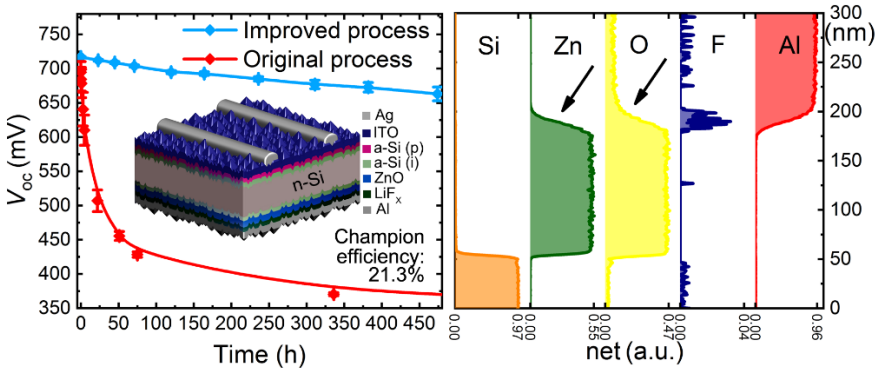

Graphical Abstract

The thicker metallization and optimal ZnO deposition (130 °C) improved device performance (21.3%-champion efficiency) and stability maintaining over 93% and 88% of the initial V_{OC} and *FF* after stored in air for 380 h. The degradation is attributed to the deterioration of LiF_x/Al work function, due to by the air ingress in LiF_x/Al interface.